Article

An Experimental and Theoretical Study of the Optical Properties of (C$_2$H$_7$N$_4$O)$_2$BiCl$_5$ for an Optoelectronic Application

Hela Ferjani [1,*], Youssef Ben Smida [2], Damian C. Onwudiwe [3,4], Nuha Y. Elamin [1,5], Safa Ezzine [6] and Norah S. Almotlaq [1]

[1] Chemistry Department, College of Science, Imam Mohammad Ibn Saud Islamic University (IMSIU), Riyadh 11623, Saudi Arabia; nyelamin@imamu.edu.sa (N.Y.E.); nsalmotlaq@imamu.edu.sa (N.S.A.)

[2] Laboratory of Valorization of Useful Material, National Centre of Research in Materials Science, University of Carthage, Technopol Borj Cedria, BP 73, Soliman 8027, Tunisia; youssef.bensmida@fst.utmcnrsm.rnrt.tn

[3] Department of Chemistry, School of Physical and Chemical Science, Faculty of Natural and Agricultural Sciences, Mafikeng Campus, North-West University, Private Bag X2046, Mmabatho 2735, South Africa; damian.onwudiwe@nwu.ac.za

[4] Material Science Innovation and Modelling (MaSIM) Research Focus Area, Faculty of Natural and Agricultural Sciences, Mafikeng Campus, North-West University, Private Bag X2046, Mmabatho 2735, South Africa

[5] Department of Chemistry, Sudan University of Science and Technology, Khartoum P.O. Box 407, Sudan

[6] Department of Chemistry, College of Sciences, King Khalid University, Abha 61413, Saudi Arabia; sezzine@kku.edu.sa

* Correspondence: hhferjani@imamu.edu.sa

Abstract: This study explores the electronic properties of (C$_2$H$_7$N$_4$O)$_2$BiCl$_5$ using the density functional theory (DFT) method, which was compared with the experimental data. The band structure of the compound indicated that it is a direct semiconductor with a band gap energy of 3.54 eV, which was comparable with the value (3.20 eV) obtained experimentally from the UV–vis spectroscopy. The density of state study showed that the conduction band was formed mainly by Bi 6p, C 2p, and N 2p states, while the valence band was formed mainly by Cl 2p, O 2p, and N 2p states. Hirshfeld surface analysis and enrichment ratio (E) were further used to investigate and quantify the intermolecular interactions within the compound. These studies established that the most important role in the stability of the structure of this crystalline material was provided by hydrogen bonding and π–π stacking interactions. The crystalline morphology of the compound was determined using BFDH simulation, based on the single-crystal structure result. Furthermore, Fourier transform infrared spectroscopy (FTIR) was used to study the vibrational modes of carbamoyl-ganidinium cations. The charge transfer process within the anionic chains of [BiCl$_5$]$_\infty$, studied using photoluminescence spectroscopy, resulted in a broad emission band with two positions of maxima centered at 336 and 358 nm. This work offers a good understanding of the optical, structural, as well as the electrical properties of (C$_2$H$_7$N$_4$O)$_2$BiCl$_5$, which are necessary in its applications in areas such as multifunctional magnetic, optoelectronic, and photonic systems.

Keywords: chlorobismuthate(III); Hirshfield surface analysis; BFDH simulation; spectroscopic studies; GGA-PBE; band structure; density of state; optical properties

1. Introduction

In recent years, organic–inorganic hybrid halometalate materials have aroused increased research interest due to their unique structural properties and wide range of potential applications [1–3]. The development of multifunctional magnetic, electronic, and luminescent systems are examples of such applications [4–6]. Among these materials,

halogenobismuthate(III), with the general formula $A_xBi_yX_z$—where A is an organic amine and X is a halogen (I, Br, Cl)—has emerged as a very important class of luminescent and semiconducting materials that has gained attention across different disciplines [7–12]. The anionic substructures of these compounds are made up of octahedral MX_6 connected by edges, corners, and faces. Due to the large number of connections, the structure ends up with discrete (0D) or numerous polymeric (1D, 2D, 3D) units [13–15]. The physical properties of the organic and inorganic components of this compound are improved by low-dimensional (1D and 0D) substructures. While the inorganic components function as semiconductors, the organic cations serve as a physical and electronic barrier. These hybrid materials could be used to improve charge carrier mobility and facilitate charge/energy transfer in high-efficiency optoelectronic and photonic devices such as solar cells, photodetection, and light-emitting diodes [16–18]. The templating effect of cations is a major factor that causes the formation of various inorganic networks. Its size and hydrogen bonds and/or van der Waals forces control the structure. Generally, non-bulky ligands with a higher delocalized charge—such as primary ammonium and guanidinium groups—could form H bonds with the terminal X atoms, and lead to anions with high X/M ratios, as observed in 1D $MIIIX_5{}^{2-}$. Another successful scheme is the inclusion of multifunctional organic cations that are able to influence the bonding topographies within the inorganic system, as well as increase orbital interaction across adjacent chains. In addition, increasing the dimensionality of the inorganic architectures and decreasing the band gap are also critical factors. We have recently been investigating the properties of halobismuthates(III) and have reported that $(C_{13}H_{28}N_2)BiCl_5$ prepared from an aqueous solution possessed 1D $BiCl_5$ anions in its structure, with an optical band gap energy of E_g = 3.51 eV [19]. An attempt to change the value of E_g by substituting chlorine with bromine and iodine in this compound was made. Unfortunately, the crystallization of the prepared (H_2TMDP) iodobismuthates was yet to be achieved. The crystallization of the cation with water molecules was most likely the leading cause of the failure.

This paper describes the experimental characterizations of $(C_2H_7N_4O)_2BiCl_5$ and its theoretical studies. The electronic band structure, total density of states (TDOS), and partial density of states (PDOS) were discussed. Furthermore, the vibrational (infrared) and optical (absorption-band gap, luminescence) properties of the compound were studied, and the results were discussed.

2. Results and Discussion

2.1. Structural Summary

The details of the single-crystal X-ray diffraction measurements and structural analysis of the compound $(C_2H_7N_4O)_2BiCl_5$ have been reported in our previous study [20]. The compound crystallizes as an organic-inorganic hybrid material with a space group of Pnma and Z = 4, and it belongs to the orthorhombic crystal system. One carbamoyl-guanidinium $(C_2H_7N_4O)^+$ cation, one bismuth atom, and four chlorine anions make up the asymmetric unit of the compound (Figure 1a). Extended one-dimensional chains of $[BiCl_5]^{2-}$ units run along the *a*-axis, separated by isolated organic cations $(C_2H_7N_4O)^+$, to form the crystal structure (Figure 1b). The 1-carbamoylguanidinium cations $((C_2H_7N_4O)_2)^{2+}$ are located around the inorganic chains and form stacks that are oriented along the *a*-axis, and are approximately parallel to each other (distanced by 3.574 (3)). The organic moieties are linked by strong N-H⋯O hydrogen bonds and π–π stacking interactions. Strong N-H⋯Cl hydrogen bonds between the organic and inorganic parts contribute to crystal cohesion. The organic cations form an insulator barrier between the semi-conductor $BiCl_6$ chains in such a packing. This periodic framework can be considered as an organic and inorganic self-organized quantum wire structure.
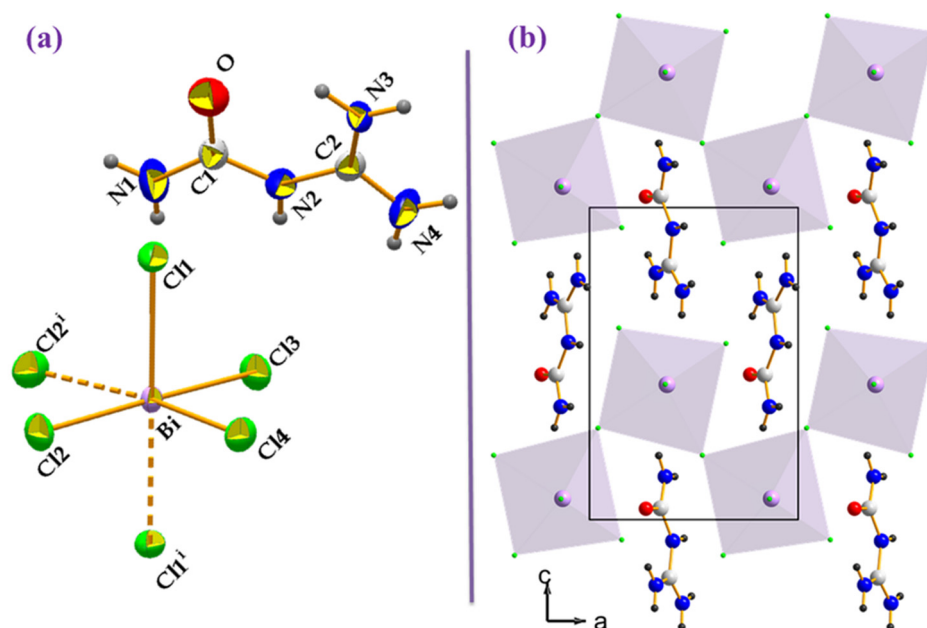
Figure 1. (**a**) Atoms numbering in $(C_2H_7N_4O)_2BiCl_5$. (**b**) Atomic arrangement of $(C_2H_7N_4O)_2BiCl_5$. The chains of corner-sharing $BiCl_6$ octahedra form the inorganic parts.

2.2. Crystal Morphology

The morphology of the crystal was elucidated by the Bravais–Friedel–Donnay–Harker (BFDH) law, which is based on a geometrical approach [21,22]. The growth rate of a particular plane is assumed to be inversely proportional to the interplanar distance in this approach (d_{hkl}). As a result, growth in a grown crystal is faster in a direction with a lower 'd_{hkl}' value. Figure 2 shows that the crystal habit was dominated by four faces—(020), (011), (101), and (111)—as revealed by the BFDH morphological prediction. Table 1 presents a summary of the results. According to the BFDH law, the larger the interplanar distance d_{hkl}, the greater the morphological importance (MI) of the corresponding hkl face. The table shows that the d_{hkl} of (020) face is the largest, with a facet area of 28.93% of total facet area, indicating that the (020) face has the greatest morphological importance (MI). The d_{hkl} of the (011) face is slightly larger than that of the (101) face, while the d_{hkl} of the (111) face is the smallest.
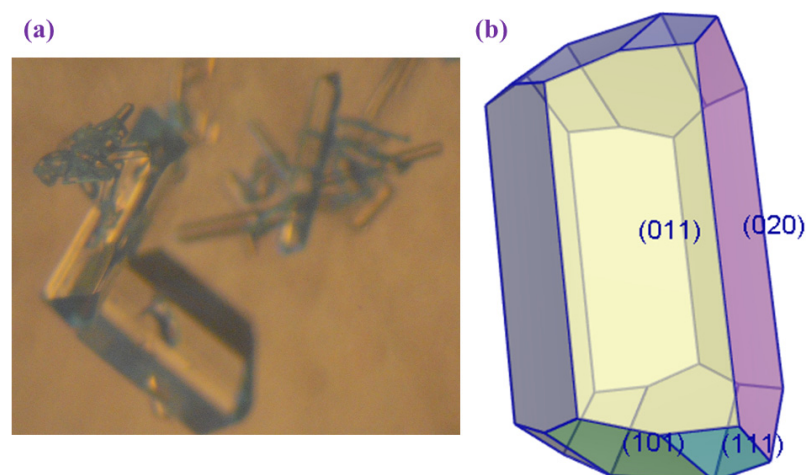

Figure 2. (**a**) Photograph of as grown $(C_2H_7N_4O)_2BiCl_5$ single crystal. (**b**) Theoretical morphology of $(C_2H_7N_4O)_2BiCl_5$ crystal based on the BFDH law.

Table 1. Calculated results of the $(C_2H_7N_4O)_2BiCl_5$ crystal based on the BFDH law.

hkl	Multiplicity	d_{hkl}	Distance	Total Facet Area	% Total Facet Area
(020)	2	10.35	9.66	817.08	28.93
(011)	4	9.73	10.27	1.148620×10^3	40.67
(101)	4	6.13	16.30	481.35	17.05
(111)	8	5.88	17.00	377.30	13.36

2.3. Hirshfeld Surface Analysis, Two-Dimensional Fingerprint Plots, and Enrichment Ratios (E)

The d_{norm}, d_e, d_i, shape index, curvedness, and fragment patch surfaces of an asymmetric unit of $(C_2H_7N_4O)_2BiCl_5$ are shown in Figure 3. Hirshfeld surfaces have been drawn over the d_{norm} 0.4629 to +1.2143 Å.
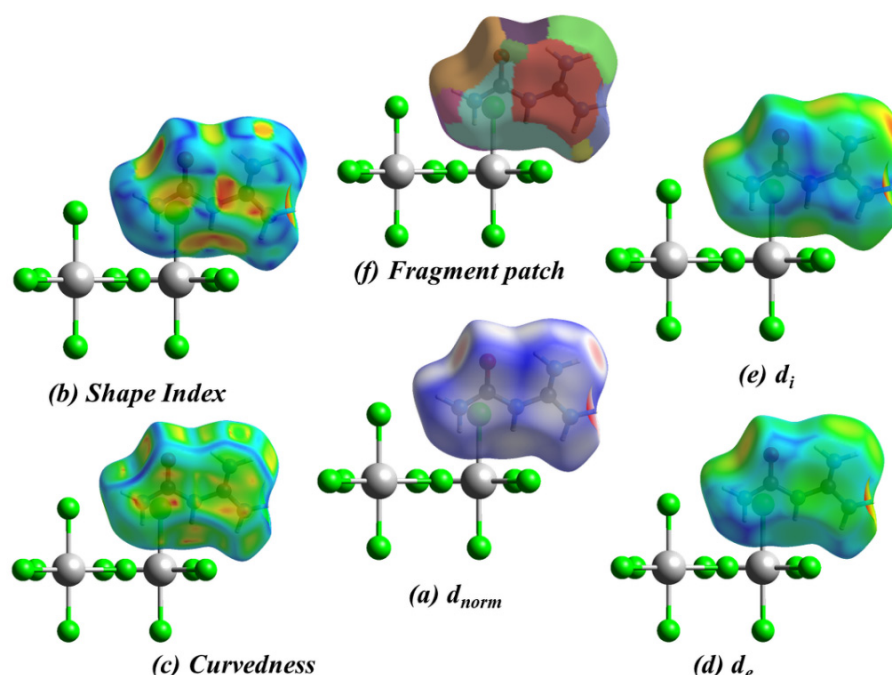
Figure 3. 3D Hirshfeld surfaces of $(C_2H_7N_4O)_2BiCl_5$ mapped with d_{norm}, shape index, curvedness, d_e, d_i, and fragment patch; (**a**) d_{norm}; (**b**) shape index; (**c**) curvedness; (**d**) d_e; (**e**) d_i; (**f**) fragment patch.

Intense red regions indicate that close contact interactions are apparent around the chlorine, nitrogen, and oxygen atoms participating in N-H⋯Cl and N-H⋯O hydrogen bonds (Table 2) [20]. The small degree of white region in d_{norm} surfaces suggests the presence of weaker and farther contact between molecules, rather than hydrogen bonds. The shape-index (Figure 3b) and curvedness (Figure 3c) provide further chemical understanding of the molecular arrangement. A surface with low curvedness designates a flat region and may be indicative of π–π stacking in the crystal. The donor and the acceptors of π–π stacking are depicted as blue and red regions around the participating atoms on the surfaces that are mapped over shape-index properties corresponding to H⋯H contacts. The nearest neighbor propensity in the surface property is indicated by the fragment patch (Figure 3f).

Table 2. Hydrogen-bond geometry for $(C_2H_7N_4O)_2BiCl_5$.

| D-H···A	D-H (Å)	H···A (Å)	D···A (Å)	D-H···A (°)
N1-H1A···Cl1 [ii]	0.86	2.607	3.271 (8)	135
N1-H1B···Cl2 [iv]	0.86	2.499	3.329 (7)	162
N2-H2···Cl4i [v]	0.86	2.702	3.524 (7)	160
N3-H3A···O [v]	0.86	2.21	3.053 (8)	167
N3-H3B··· O	0.86	2.08	2.734 (8)	132
N4-H4A···Cl1 [vi]	0.86	2.525	3.347 (7)	160
N4-H4B···Cl4 [iv]	0.86	2.594	3.421 (7)	162

Symmetry codes: ([ii]) x − 1/2, y, −z + 3/2; ([iv]) x − 1, y, z; ([v]) −x + 1, −y + 1, −z + 1; ([vi]) x − 1/2, y, −z + 1/2.

The overall fingerprint plot was calculated, including all intermolecular contacts, as well as the decomposed fingerprint plots, which focus on specific interactions. The 2D fingerprint plot for $(C_2H_7N_4O)_2BiCl_5$ is shown in Figure 4 with the relative percentage contributions to the overall Hirshfeld surface, and those defined into Cl···H (28.7%) and H···H (25.3%) as the most abundant interactions, followed by N···H (14%) and O-H (12%) as the second abundant and least abundant interactions, respectively. The relative percentage contributions to the overall Hirshfeld surface are presented in the Figure 5.
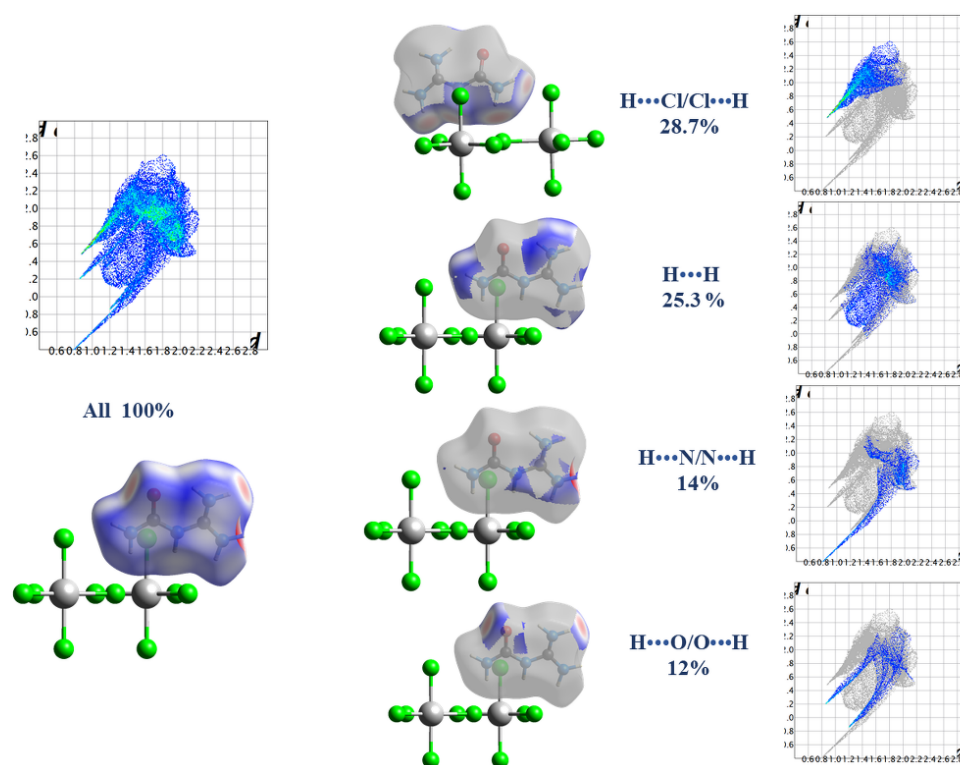
Figure 4. The full 2D fingerprint plot for $(C_2H_7N_4O)_2BiCl_5$ and fingerprint plots delineated into H···H, Cl···H, N···H, and O···H contacts.
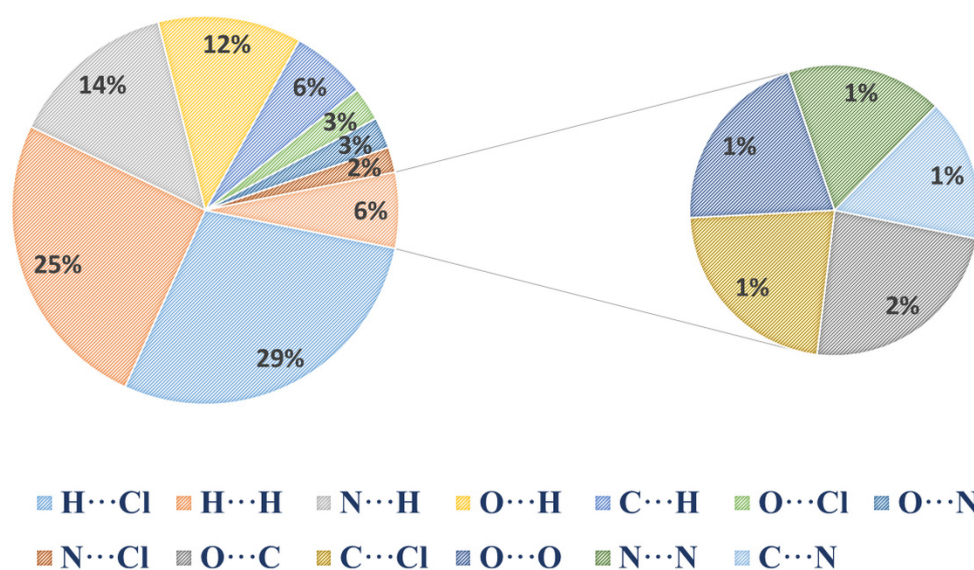
**Figure 5.** Histogram of different intermolecular contacts to the Hirshfeld surface area in $(C_2H_7N_4O)_2BiCl_5$.

The H$\cdots$Cl, O$\cdots$Cl, N$\cdots$H, O$\cdots$O, C$\cdots$H, N$\cdots$O, and O$\cdots$H contacts—as well as H$\cdots$O contacts—are highly favored in the structure since the corresponding enrichment ratios E_{HCl}, E_{OCl}, E_{HN}, E_{OO}, E_{CH}, E_{NO}, and E_{OH} are larger than unity (1.47–1) (Table 3). Contrarily, the H$\cdots$H contacts on the surface are less favored ($E_{HH} = 0.81$). This is due to a relatively higher amount of random contact R_{HH}, despite the molecule being characterized by a high amount of SH. Interestingly, the C$\cdots$O contacts in the structure are remarkably enriched ($E_{CO} = 1.36$). This could be ascribed to the significantly higher amount of C$\cdots$O contacts on the molecular surface, together with a lower number of random contacts (R_{CO}) (Table 3).

Table 3. Percentage contributions of interactions, surface contacts (S_X), random contacts (R_{XX}/R_{XY}), and enrichment ratios (E_{XX}/E_{XY}) for $(C_2H_7N_4O)_2BiCl_5$.

Atoms	H	C	N	O	Cl
H	25.3	-	-	-	-
C	6.3	/	-	-	-
N	14	1	1.1	-	-
O	12	1.5	2.6	1.3	-
Cl	28.7	1.4	2.1	2.8	0
Surface %	55.8	5.1	10.95	10.75	17.5
Random Contacts (R_{XX} and R_{XY})					
H	31.14	-	-	-	-
C	5.69	0.26	-	-	-
N	12.22	1.12	1.20	-	-
O	12	1.10	2.35	1.16	-
Cl	19.53	1.79	3.83	3.76	3.06
Enrichment Ratio E					
H	0.81	-	-	-	-
C	1.11	/	-	-	-
N	1.15	0.89	0.91	-	-
O	1	1.36	1.11	1.12	-
Cl	1.47	0.78	0.55	0.74	/

2.4. Vibrational Properties

All assignments were derived from the spectra of the carbamoyl-guanidinium (+1) cation reported in previous studies [23–25]. The results arerepresented in Figure 6 and summarized in Table 4.
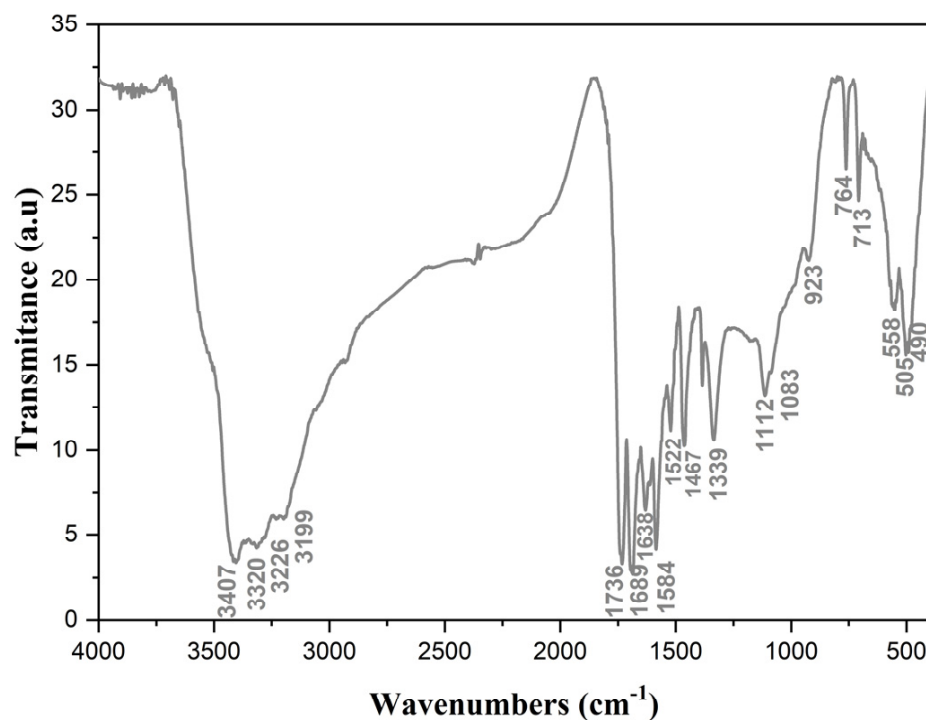
Figure 6. Infrared spectrum of $(C_2H_7N_4O)_2BiCl_5$ recorded at room temperature.

In the high wavenumber region of the IR spectrum (2500–3500 cm^{-1}), the strong intensity peak corresponds to the stretching vibrations of NH_2 and NH groups (3407, 3320, 3226, and 3199 cm^{-1}). The strong hydrogen-bond interactions involving the amino groups (with lengths ranging from 2.734 to 3.524) are indicated by the broad nature of this band. At 1736 and 1584 cm^{-1}, the $-NH_2$ bending modes were identified. The amino groups relating to the guanidinium ion fragment, (NH_2) guanidine, have a higher frequency than the primary amine, (NH_2) belonging to the ureic group, which has a lower frequency [23]. The band identified at 1689 cm^{-1} was attributed to the stretching vibrations of the carbonyl group, $\upsilon(CO)$. The two amino groups show two distinct bands ascribed to the rocking vibrations at 1112 and 1083 cm^{-1}, which are associated with the amino groups of the guanidine moiety and the primary amino group of the amide, respectively. Furthermore, as shown in the similar spectrum of guanidine, the band at 1339 cm^{-1} has been assigned to the bending vibration of the amine, $\delta(NH)$ [26]. Stretching $\upsilon(CN)$ of the amide group, a characteristic band for primary amides in this spectral region, has been assigned to the band at 1467 cm^{-1}. The vibrational bands located at 1638, 1522, and 923 cm^{-1} have been attributed to the characteristic vibrations of guanidine skeletal modes, which agree with the previously reported spectra [23–26]. The bands recorded at 490, 505, 584, 713, and 764 cm^{-1} were assigned to the mixed $\rho(NCN)$, υCN, and $\omega(NH_2)$ vibrations of carbamoylguanidinium cations [24–27].

**Table 4.** Observed infrared positions (cm^{-1}) of $(C_2H_7N_4O)_2BiCl_5$.

Observed Wavenumbers (cm^{-1})	Guanylurea Hydrochloride [27]	Assignments
3407	3408	$\nu_{as}(NH_2)$, $\nu_s(NH_2)$
3320	3320	
3220	3230	$\nu(NH)$
3199	3152	
1736	1736	$\delta(NH_2)$Guanidine
1689	1672	$\nu(CO)$Amide
1638	1638	$\nu(C=N)$
1584	1583	$\delta(NH_2)$ Amide
1522	1523	$\nu_a(NCN)$
1467	1460	$\nu(CN)$Amide
1339	1341	$\delta(NH)$
1112	1117	$\rho(NH_2)$
1083	1057	
923	932	$\nu_s(NCN)$
764–713	756–716	$\omega(NCN)/\delta(NCN)$
558–505	535	$\omega(NH_2)$
490	448	$\rho(NCN)$
	428	

Abbreviations and symbols: ν: stretching; δ: deformation; ρ: rocking; ω: wagging; τ: torsion; s: symmetric; as: antisymmetric.

2.5. UV–Visible Spectrum

In the room-temperature UV–visible absorption spectrum, three distinct absorption bands centered at 225, 324, and 364 nm can be observed (Figure 7a). These bands are assigned typically to either metal-centered (MC) transitions [28–30] or to ligand-to-metal charge transfer transitions [31,32]. On the other hand, the planar conjugated carbamoyl-guanidinium cations always show a n-π* absorption band around 225 nm as reported by other studies [33,34]. In the current study, the first band at 225 nm was assigned to the n-π* transition within the carbamoyl-guanidinium cation.
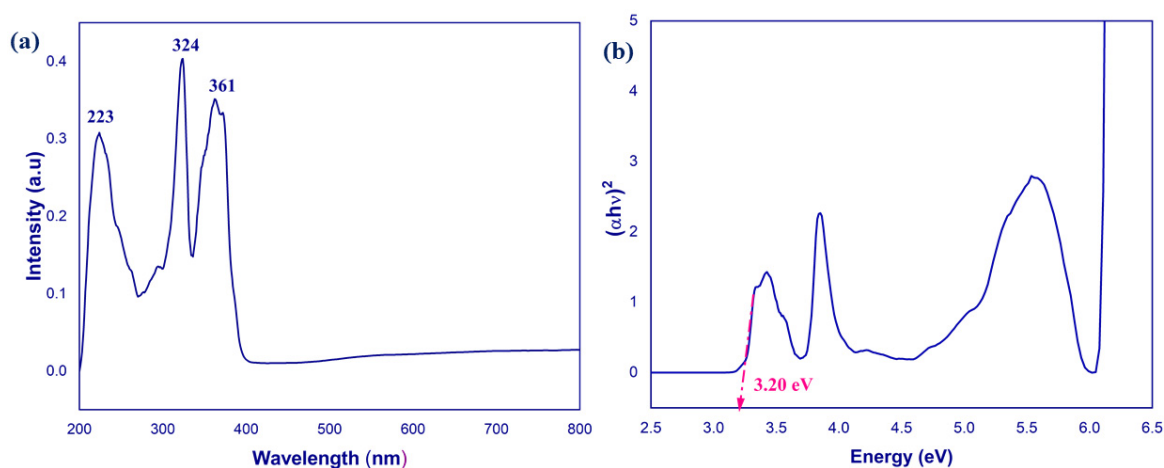
Figure 7. (**a**) Room temperature UV–vis absorption spectrum. (**b**) Tauc plot of $(C_2H_7N_4O)_2BiCl_5$.

The bands centered at around 324 and 364 nm were generated by the metal-centered (MC) transition and ligand-to-metal charge transfer (LMCT) transition.

The optical band gap of $(C_2H_7N_4O)_2BiCl_5$ was determined by measuring the UV–visible diffuse reflectance spectrum at room temperature. The absorbance as a function of reflectance presented by Kubelka–Munk is given in Equation (1):

$$F(R) = \alpha = (1 - R)/(2R) \tag{1}$$

Extrapolation of the linear portion of the absorption edges (Figure 7b) yielded an energy band gap of 3.20 eV, indicating that the title compound is a semiconductor.

2.6. Photoluminscence Spectrum

Solid-state room temperature photoluminescence spectrum of $(C_2H_7N_4O)_2BiCl_5$ was recorded at an excitation wavelength of 275 nm. As shown in Figure 8, $(C_2H_7N_4O)_2BiCl_5$ shows a broad violet emission in the range of 300–400 nm with peaks centered at 336 and 358 nm. These peaks could be assigned to electronic transition within the inorganic part of chlorobismuthate(III) [35–37]. In general, the photoluminescence emission of the bismuth(III) is dependent on the s2 electron. The chloride 2p in octahedral bismuth chloride centers is excited to the bismuth 6p/chloride 3s, resulting in a HOMO–LUMO transition [37].
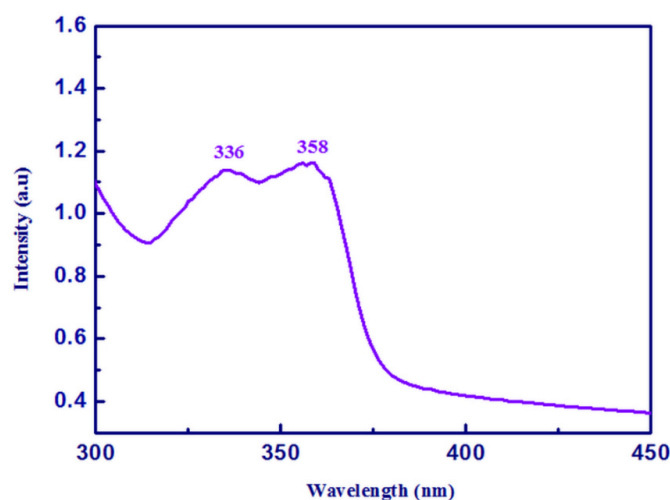
Figure 8. Solid-state emission spectrum of $(C_2H_7N_4O)_2BiCl_5$ upon an excitation at 270 nm.

2.7. Electronic Structure

The density of states (partial and total) of a material or compound, along with its band structure, is a suitable tool in the prediction of its physical properties such as electrical resistivity and optical absorption, as well as understanding the physics of the materials in solid-state devices. Using the GGA approximation with norm-conserving pseudopotential in reciprocal space, the band structure, partial density, and total density of states were explored. Figure 9 shows the simulated band gap structure of $(C_2H_7N_4O)_2BiCl_5$. The calculated energy gap was $E_g = 3.543$ eV. This result demonstrates the accuracy of the current calculations and shows that the GGA-PBE method is in good agreement with the experimental value. It is evident from Figure 9b that the maximum of the valence band and the minimum of the conduction band are in the same direction X, indicating that it is a direct conduction band.
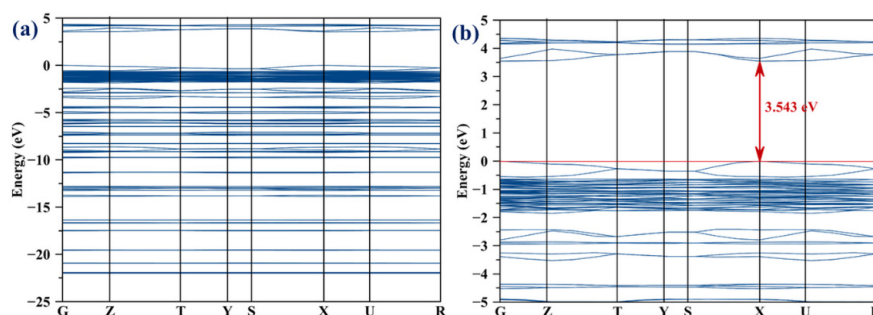
Figure 9. Electronic band structure of $(C_2H_7N_4O)_2BiCl_5$: (**a**) overall view, (**b**) enlarged view.

The partial density of states (PDOS) and total density of states (DOS) diagrams in Figure 10 could be used to determine the composition of the calculated bands. The mixed contribution of bismuth 5d orbitals, carbon (2s, 2p orbitals), nitrogen (2s orbital), oxygen (2s, 2p orbitals), and hydrogen make up the lowest part of the valence band (VB) between −23 and −15 eV. The electronic cloud around the N-H, O-H, and C-H bands are responsible for this result. The mixed states (6s, 6p) of bismuth, (3p, 3s) of chlorine, (2s, 2p) of carbon, (2s, 2p) of oxygen, and hydrogen make up the maximum of the valence band (MVB). The orbital 6p of bismuth, 3p of chlorine, 2p of oxygen, 2p of nitrogen, and 2p of carbon make up the minimum of the conduction band (MCB).
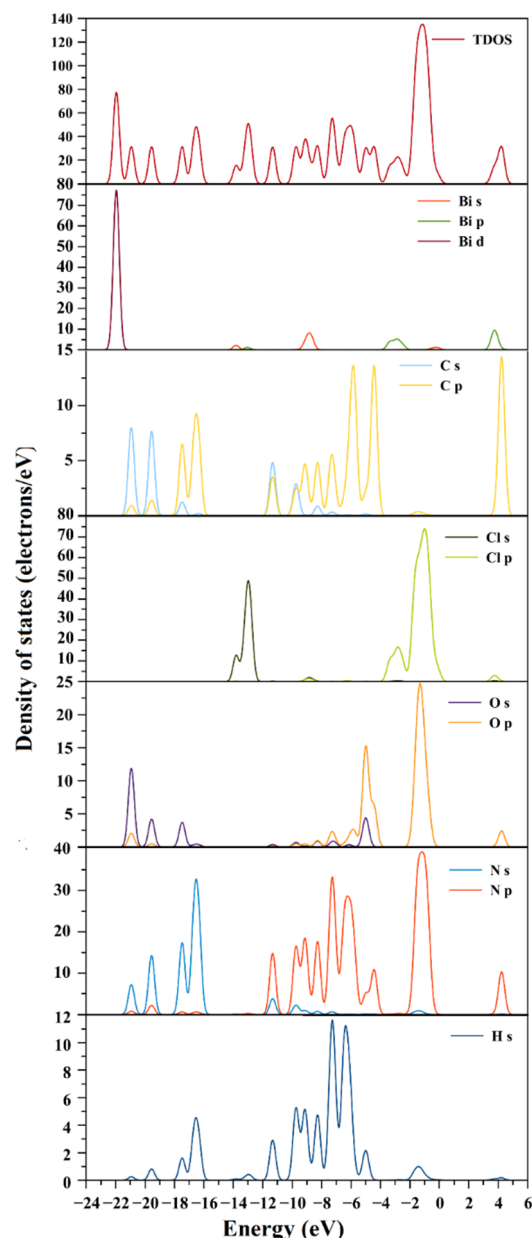
Figure 10. Total and partial densities of states for $(C_2H_7N_4O)_2BiCl_5$ using GGA/PBE functional.

2.8. Optical Properties

The most important function that describes the optical properties of a material is the dielectric function $\varepsilon(\omega)$ which characterizes the interaction between electromagnetic waves and electrons [38].

Thus, the dielectric function connects the electronic structure of material to the physical process of the transition. Then, the other optical spectrum (refractive index, reflectivity, absorption, loss function energy, optical conductivity) can be deduced through it. The dielectric function $\varepsilon(\omega)$ can be written as [39]

$$\varepsilon(\omega) = \varepsilon_1(\omega) + i\varepsilon_2(\omega) \tag{2}$$

where $\varepsilon_1(\omega)$ and $\varepsilon_2(\omega)$ are the real (dispersive) and the imaginary (absorptive) parts respectively [40]. The imaginary part of the dielectric function $\varepsilon_2(\omega)$ represents the absorption within the system when light of a specific frequency is used. $\varepsilon_2(\omega)$ can be calculated from direct numerical evaluations of the momentum matrix elements of the electric dipole operator between the conduction and valence band wave functions [41]

$$\varepsilon_2(\omega) = \left(\frac{2e^2\pi}{\omega\varepsilon_0}\right)\sum_{kvc}|\langle\psi_k^c|\boldsymbol{u}.\boldsymbol{r}|\psi_k^v\rangle|^2\delta(\mathrm{E}_k^c - \mathrm{E}_k^v - E) \tag{3}$$

where $\boldsymbol{u}$ is the polarization vector of the incident electric field, $\boldsymbol{r}$ is the electron's radius vector, and e is electric charge, ψ_k^c and ψ_k^v are the conduction and valence band wave functions at k, respectively, and ε_0 is the vacuum permittivity. The summation of the equation is applied over all states from the occupied and empty bands, with their wave functions are obtained in a numerical form after the optimization of the crystal structure.

The real part, $\varepsilon_1(\omega)$, of the dielectric function is linked to the polarization of the material. It can be obtained from the imaginary part by using the Kramers–Krönig dispersion equation [41,42]

$$\varepsilon_1(\omega) = 1 + \frac{2}{\pi}p\int_0^\infty \frac{\omega'\varepsilon_2(\omega')d\omega'}{\omega'^2 - \omega^2} \tag{4}$$

where p is the principal value of the integral.

In addition, the other optical properties can be derived from the real $\varepsilon_1(\omega)$ and imaginary $\varepsilon_2(\omega)$ of the dielectric function such as [41,42].

The refractive index $n(\omega)$ and the extinction coefficient $k(\omega)$:

$$n(\omega) = \frac{\sqrt{\varepsilon_1^2(\omega) + \varepsilon_2^2(\omega)} + \varepsilon_1^{1/2}(\omega)}{\sqrt{2}} \tag{5}$$

$$k(\omega) = \frac{\sqrt{\varepsilon_1^2(\omega) + \varepsilon_2^2(\omega)} - \varepsilon_1^{1/2}(\omega)}{\sqrt{2}} \tag{6}$$

The optical reflectivity $R(\omega)$:

$$R(\omega) = \left|\frac{\sqrt{\varepsilon_1(\omega) + j\varepsilon_2(\omega)} - 1}{\sqrt{\varepsilon_1(\omega) + j\varepsilon_2(\omega)} + 1}\right|^2 \tag{7}$$
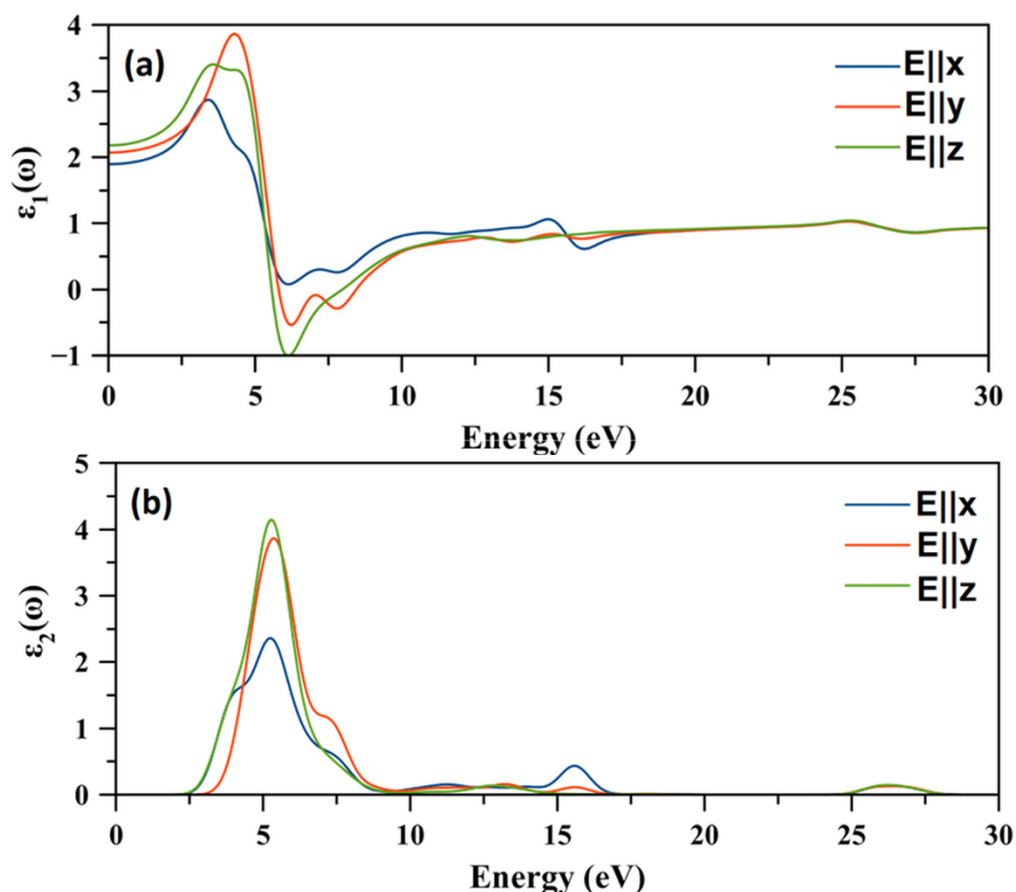
Energy-loss spectrum $L(\omega)$:

$$L(\omega) = \frac{\varepsilon_2(\omega)}{\varepsilon_1^2(\omega) + \varepsilon_2^2(\omega)} \tag{8}$$

Absorption coefficient $\alpha(\omega)$:

$$\alpha(\omega) = \sqrt{2}\left[\sqrt{\varepsilon_1^2(\omega) + \varepsilon_2^2(\omega)} - \varepsilon_1(\omega)\right]^{1/2} \tag{9}$$

All optical properties were calculated with calculation geometry polycrystalline, instrumental smearing 0.5 eV.

The real part $\varepsilon_1(\omega)$ and the imaginary part $\varepsilon_2(\omega)$ of the dielectric function with polarized radiation along the [100], [010], and [001] directions are shown in Figure 11.


Figure 11. Variation of (**a**) the real part $\varepsilon_1(\omega)$ and (**b**) the imaginary part $\varepsilon_2(\omega)$ of the dielectric function as function of the energy of the $(C_2H_7N_4O)_2BiCl_5$ compound.

The three plots of the real parts of the dielectric function are different. This proves that the optical properties of the compound are anisotropic. The estimated electronic static dielectric function $\varepsilon_1(0)$ is $\varepsilon_{1\,xx}(0) = 1.89$, $\varepsilon_{1\,yy}(0) = 2.08$, and $\varepsilon_{1\,zz}(0) = 2.18$. The square root of the static dielectric constant may provide an estimation of the refractive index. The $\varepsilon_1(\omega)$ plots increase with the increasing of the photon energy from their static values and then reach maximum values of $\varepsilon_1(\omega)$ of about $\varepsilon_{1\,xx}(\omega) = 2.87$ at 3.39 eV, $\varepsilon_{1\,yy}(\omega) = 3.87$ at 4.29 eV, and $\varepsilon_{1\,zz}(\omega) = 3.40$ at 3.56 eV following its decrease. A rather steep decrease is observed for $\varepsilon_1(\omega)$, then it becomes negative. The negative values of the real part of the dielectric function are due to damping of the electromagnetic wave, and zero values indicate that the longitudinally polarized waves are possible.

The imaginary parts of the dielectric function started at 2.16 eV, 2.45 eV, and 1.75 eV for $\varepsilon_{2\,xx}(\omega)$, $\varepsilon_{2\,yy}(\omega)$, and $\varepsilon_{2\,zz}(\omega)$ respectively (Figure 11b). Since the spectrum of the imaginary part $\varepsilon_2(\omega)$ is related to the absorption of the radiation from the material, it was possible to determine the origin of the spectrum peaks based on the density of states curves. This implies that there was transition from valence sub-bonds to the conduction sub-band. The unpolarized dielectric function curves of the $(C_2H_7N_4O)_2BiCl_5$ are plotted in Figure 12, which shows the presence of at least six electronic transitions (Figure 12). The same transition bands—such as E1, E2, and E3—are overlapped. A careful examination of

the partial state densities (Figure 9) and the $\varepsilon_2(\omega)$ spectrum (Figure 12) and by following the selection rules could determine the nature of different transitions [34].
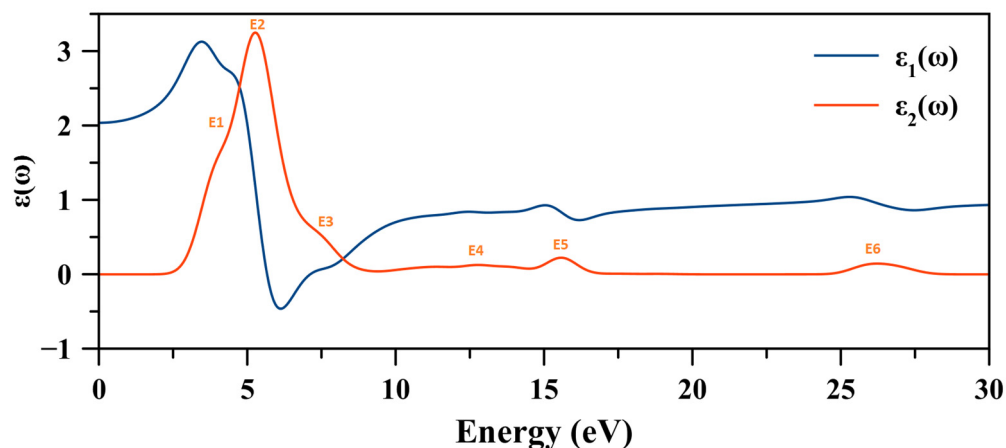
Figure 12. Variation of the unpolarized real and imaginary parts of the dielectric function showing the presence of six transitions.

The refractive index of a material characterizes the modification of the propagation of light waves by their interaction with the material's medium in which they propagate. Figure 13 shows the variation of the refractive index and the extinction coefficient of $(C_2H_7N_4O)_2BiCl_5$ as a function of energy of the material in the orthorhombic system and along the three crystallographic directions.
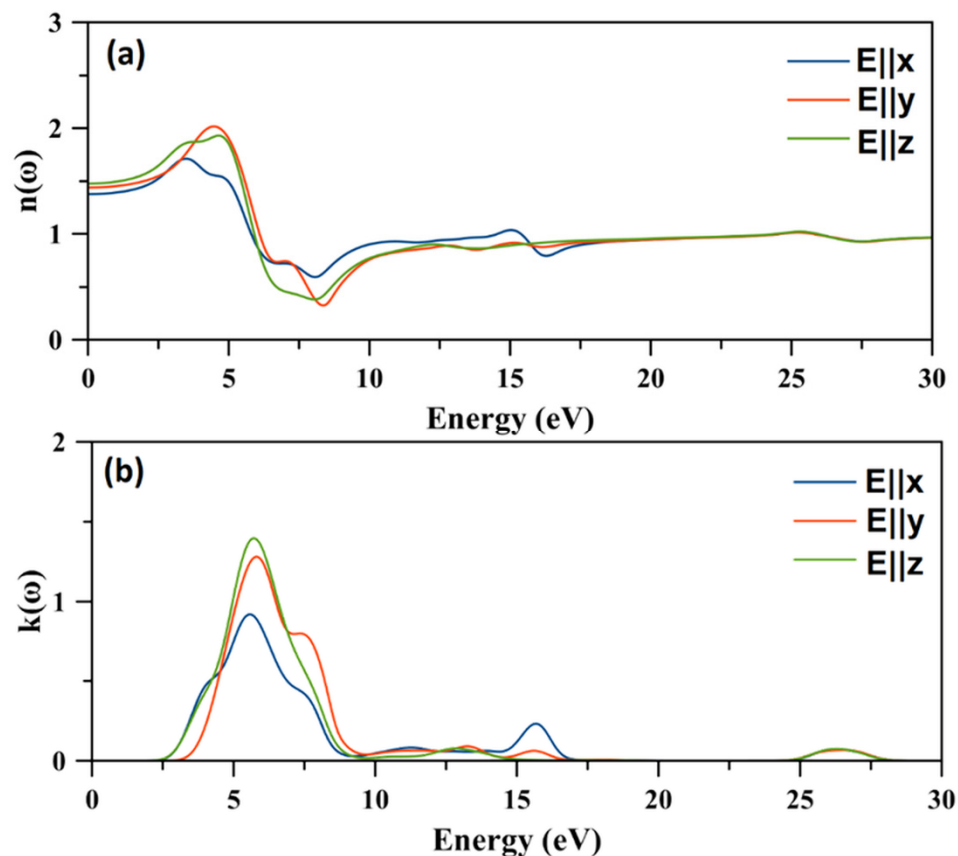
Figure 13. Variation of (**a**) the refractive index $n(\omega)$ and (**b**) the extinction coefficient $k(\omega)$ as a function of the energy of the $(C_2H_7N_4O)_2BiCl_5$ compound.

The refractive index $n(\omega)$ (Figure 13a) exhibited some anisotropy in the energy range 0–20 eV. $n(\omega)$ started from the static refractive index $n(0)$, which are 1.37, 1.44, and 1.48 along the [100], [010], and [001] directions respectively. The static refractive index $n(0)$ is related to the static dielectric function $\varepsilon_1(0)$ by the relation $n = \sqrt{\varepsilon\mu}$, where μ is the relative permeability which is equal to the unit for nonmagnetic substances. Thus, for the compound, $n = \sqrt{\varepsilon}$. Then, $n(\omega)$ increased with an increase in the energy from the static value to reach a maximum of about 1.71, 2.02, and 1.92 at 3.48 eV, 4.47 eV, and 4.65 eV along the [100], [010], and [001] directions respectively. In this energy range, the more the refractive index increased, the more the light beam was refracted. Afterwards, $n(\omega)$ decreased rapidly to reach a minimum. By comparison, the spectra of the refractive index $n(\omega)$ and real part of the dielectric function $\varepsilon_1(\omega)$ were very similar.

Figure 13b shows the variation of the extinction coefficient $k(\omega)$ as a function of the energy of the $(C_2H_7N_4O)_2BiCl_5$. We observed that, in the ~6–~8 eV energy range, the extinction coefficient $k(\omega)$ was greater than the refractive index $n(\omega)$ in the [010] and [001] directions, which indicated that the light in this energy region was not able to propagate in the material.

The optical reflectivity $R(\omega)$ is defined as the fraction of light reflected at an interface. Figure 14 shows the energy-dependent reflectivity spectrum of $(C_2H_7N_4O)_2BiCl_5$ along the three crystallographic directions.
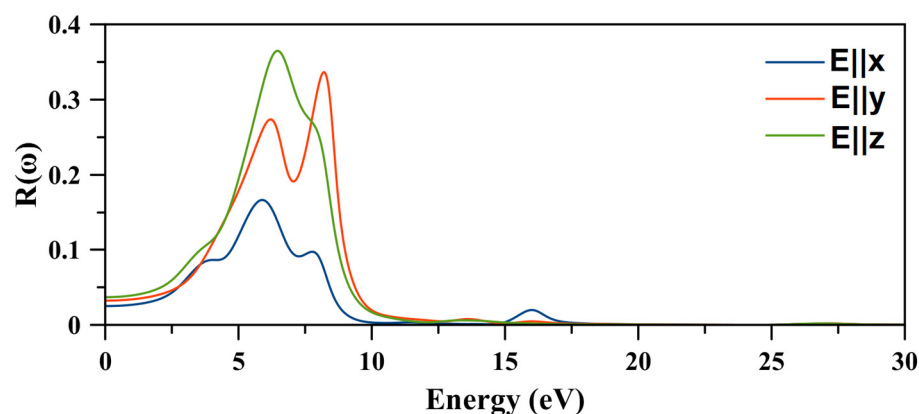
Figure 14. Variation of the optical reflectivity as a function of the energy of the $(C_2H_7N_4O)_2BiCl_5$ compound.

The static reflectivity was about 4% along the three crystallographic directions. Then, the reflectivity varied slightly but remained below 3 eV. Afterwards, the reflectivity increased rapidly and reached a maximum in the 6–9 eV energy range. Then, the reflectivity became almost zero. The reflectivity had the lowest value along the [100] direction in the 0–10 eV energy range, where the maximum value did not exceed 15%. However, the maximum values of the reflectivity were about 36% along the [001] direction.

The absorption coefficient $\alpha(\omega)$ quantifies the energy of an electromagnetic wave of frequency (ω), absorbed per unit length of medium, where it propagates. Figure 14 shows the energy dependent absorption coefficient spectrum of the $(C_2H_7N_4O)_2BiCl_5$ in an energy range of up to 30 eV for incident electromagnetic radiation polarized parallel to crystallographic directions.

The general overall features of the absorption spectra of the three radiation directions were different, which means the anisotropy of the medium is consistent with the orthorhombic system. Note that the two curves along the [100] and [001] directions started at the same absorption and grew rapidly at the same rate. However, the curve along [010] is shifted. This indicated that the band edge was anisotropic.

Figure 15 shows that $(C_2H_7N_4O)_2BiCl_5$ is an absorber both in the visible and UV lights. Indeed, the absorption occurs between 3 and 17 eV with six peaks where the first three peaks were overlapped. In the 2–10 eV energy range, the [001] direction exhibited the

highest $\alpha(\omega)$ value which reached about 1.3×10^5 cm^{-1}, while the [100] direction has the smallest value at 0.8×10^5 cm^{-1}. However, in the 10–17 eV energy range, the [100] direction exhibited the highest absorption value of 0.6×10^5 cm^{-1} at 16 eV. The maximum value of the absorption coefficient of the title compound is very similar to the well-known lead halide perovskites $CH_3NH_3PbX_3$ (X = I, Br, Cl) [43–45].
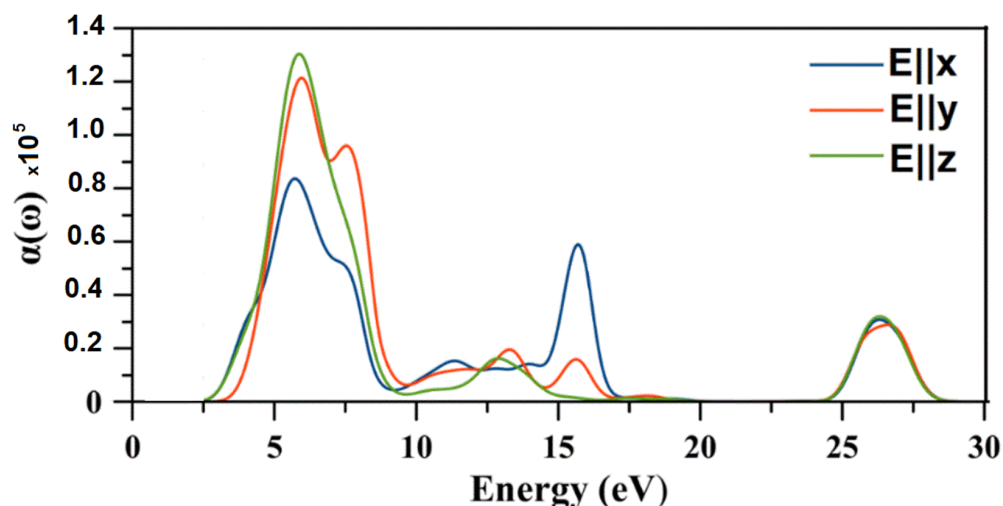
Figure 15. Variation of the absorption coefficient as a function of the energy of the $(C_2H_7N_4O)_2BiCl_5$ compound.

The electron energy loss function $L(\omega)$ is an important optical parameter which describes the energy lost by the free charge carriers (absorbed) during the course of passing through a homogeneous material. The energy loss spectrum of the $(C_2H_7N_4O)_2BiCl_5$ compound is presented in Figure 16.
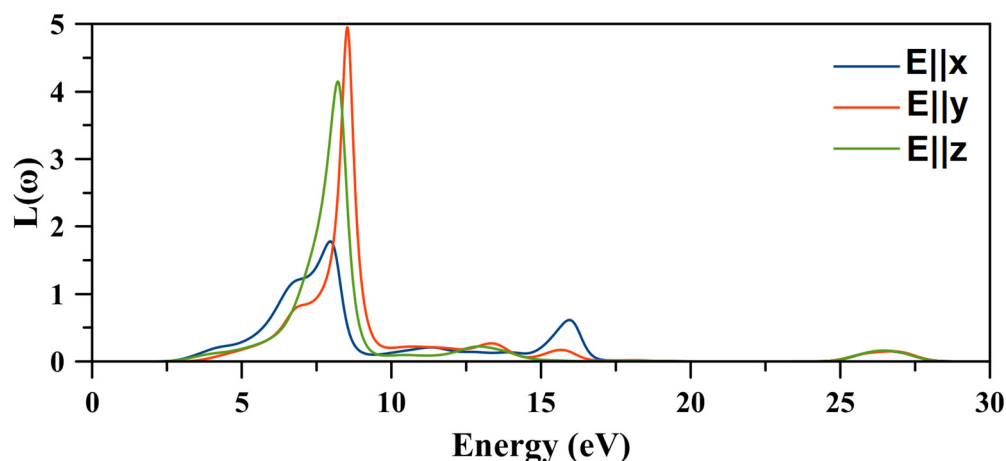
Figure 16. Energy-loss spectrum of the $(C_2H_7N_4O)_2BiCl_5$ compound.

The significant peaks were located at 7.95, 8.52, and 8.21 eV for [100], [010], and [001] directions respectively, where electrons were originally unbound to their lattice sites and started the plasma oscillation. It was evident that the dielectric energy loss was more pronounced according to the [010] direction and was the weakest according to the [100] direction. The maximum of the electron energy loss function corresponded to the abrupt decline of the reflection magnitude [46].

3. Materials and Methods

3.1. Materials

Bismuth chloride ($BiCl_3$) and cyanoguanidine ($C_2H_4N_4$) (molar ratio 1:2) was dissolved in 20 mL of absolute ethanol and an excess of HCl was added to the solution. The mixture was stirred, then kept at room temperature. After three months, colorless single crystals were obtained and isolated from the reaction.

3.2. Physical Measurements

Fourier-transform infrared spectroscopy (FT-IR) spectrum of the compound was measured at room temperature in the range of 4000–400 cm^{-1} on a Perkin-Elmer Paragon 1000 Pc spectrometer (Sacramento, CA, USA). The sample for the FTIR analysis was prepared by dispersing 2% of the compound in KBr discs. A Perkin-Elmer Lambda 45 UV–visible absorption spectrometer was used to measure the optical absorption spectrum at room temperature. A HORIBA JOBIN-YVON (HR320) spectrometer (Piscataway, NJ, USA) was used to record the photoluminescence spectrum, while a diode laser with a wavelength of 270 nm was used to excite the sample.

3.3. Computational Details

All first principal calculations were carried out based on the density functional theory (DFT) method by employing the pseudopotential plane wave as implemented in CASTEP code [30,47]. The crystallographic data of $(C_2H_7N_4O)_2BiCl_5$, determined by single X-ray diffraction, have been used as starting sets. The electronic exchange-correlation energy (XC) was treated using the generalized gradient approximation (GGA) together with the Perdew–Burke–Ernzerhof (PBE) parameterization [48]. The norm-conserving pseudopotential was used to describe the ionic core and valence electron interactions. The plane wave basis set had a 400-eV energy cut-off, and a $2 \times 2 \times 2$ special Monkhorst-Pack [49] k-point mesh for the Brillouin zone (BZ) was adopted. The Broyden–Fletcher–Goldfarb–Shannon (BFGS) algorithm was used to determine the minimum energy of the crystal structure. The atomic force, maximum displacement, and total energy convergence criteria were 0.05 eV $Å^{-1}$, 0.002 Å, and 10^{-6} eV, respectively.

3.4. Hirshfeld Surfaces Analysis, Enrichment Ratio (E), and Morphology Simulation

CrystalExplorer17 was used to create the Hirshfeld surfaces [50] and their corresponding 2D fingerprint plots [51] with a final refined crystallographic information file as the input. The intercontact in the crystal packing was quantified and decoded using d_{norm} (normalized contact distance) and 2D fingerprint plots, respectively. The short interatomic contacts created the dark-red spots on the d_{norm} surface, while the other intermolecular interactions caused light-red spots. The d_i (inside) and d_e (outside) symbolize the distances from the nuclei to the Hirshfeld surface in terms of relative van der Waals radii. The color gradient (blue to red) in the fingerprint plots depicts the proportional contribution of intercontact over the surface.

The enrichment ratio (E) [52] was used to analyze the tendency of the pair of elements (X, Y) to form contacts in the crystals. E is the proportion of actual contacts in the crystal compared to random contacts (theoretical proportion). If E > 1, pairs of elements will have a greater chance of developing contacts in crystals; and if E < 1, the pairs will avoid making contact. The input values for both types (one type and two types of chemical elements) to the E was derived from the CrystalExplorer17 software.

The Materials Studio program [53] was used to predict the morphology of the $(C_2H_7N_4O)_2BiCl_5$ material. As input, a crystallographic information file (cif) is provided.

4. Conclusions

The present work describes the spectroscopic and morphological characterization of chlorobismuthate $(C_2H_7N_4O)_2BiCl_5$ by both experimental and theoretical approaches. In the theoretical study, the intermolecular interactions were explored using Hirshfeld surface

analysis and enrichment ratio (E), which showed that the most important role in the stability of the crystal structure was provided by hydrogen bonding and π–π stacking interactions. The highest value of E was calculated for the contact Bi$\cdots$Cl (2.53), followed by N$\cdots$N (2.17), and there was a high tendency to form contacts in the crystal. This provided the basis for the existence of the π–π stacking interactions in the structure. The crystal growth morphology of $(C_2H_7N_4O)_2BiCl_5$ was predicted by the BFDH model, which showed that (020) and (011) faces of the crystal were the main growth faces. The vibrational modes of the organic cation present in the structure were assigned using the experimental IR spectrum, while the optical properties were studied by optical absorption and photoluminescence measurements. The results revealed that the band gap of this compound was 3.20 eV and that it exhibited a broad violet emission band in the violet range centered at 336 and 358 nm. The theoretical determination of the optical properties shows that the title compound was a direct semiconductor. The dielectric function shows six electronic transitions. The absorption spectrum indicates that the $(C_2H_7N_4O)_2BiCl_5$ material is an absorber in the 3–10 eV energy range with a maximum of 1.3×10^5 cm^{-1}.

Author Contributions: Conceptualization, H.F. and Y.B.S.; Methodology, H.F.; Software, H.F. and Y.B.S.; Validation, H.F. and Y.B.S.; Data curation, Formal analysis, Investigation, Methodology, Validation, S.E., N.Y.E. and N.S.A.; Investigation, H.F.; Resources, H.F.; Data curation, H.F., D.C.O. and Y.B.S.; Writing—original draft preparation, H.F. and Y.B.S.; Writing—review and editing, H.F., D.C.O. and Y.B.S.; Visualization, H.F. and Y.B.S.; Supervision, H.F. and D.C.O.; Project administration, H.F.; Funding acquisition, H.F. All authors have read and agreed to the published version of the manuscript.

Institutional Review Board Statement: Not applicable.

Informed Consent Statement: Not applicable.

Conflicts of Interest: The authors declare no conflict of interest.

References

1. Trabelsie, S.; Samet, A.; Dammak, H.; Michaud, F.; Santos, L.; Abid, Y.; Chaabouni, S. Optical properties of a new luminescent hybrid material $[C_6N_2H_5]_3BiCl_6$ involving a resonance energy transfer (RET). *Opt. Mater.* **2019**, *89*, 355–360. [CrossRef]
2. Barkaoui, H.; Abid, H.; Yangui, A.; Triki, S.; Boukheddaden, K.; Abid, Y. Yellowish white-light emission involving resonant energy transfer in a new one-dimensional hybrid material:$(C_9H_{10}N_2)$ $PbCl_4$. *J. Phys. Chem. C* **2018**, *122*, 24253–24261. [CrossRef]
3. Kotov, V.Y.; Ilyukhin, A.B.; Baranchikov, A.E.; Ishmetova, R.I.; Rusinov, G.L.; Kozyukhin, S.A. Synthesis, crystal structure and optical properties of 1,1′-(1,n-alkanediyl)bis(3-methylimidazolium) halobismuthates. *J. Mol. Struct.* **2018**, *1151*, 186–190. [CrossRef]
4. Mitzi, D.B.; Brock, P. Structure and optical properties of several organic−inorganic hybrids containing corner-sharing chains of bismuth iodide Octahedra. *Inorg. Chem.* **2001**, *40*, 2096–2104. [CrossRef]
5. Hassen, S.; Chebbi, H.; Arfaoui, Y.; Robeyns, K.; Steenhaut, T.; Hermans, S.; Filinchuk, Y. Spectroscopic and structural studies, thermal characterization, optical proprieties and theoretical investigation of 2-aminobenzimidazolium tetrachlorocobaltate (II). *Spectrochim. Acta Part A Mol. Biomol. Spectrosc.* **2020**, *240*, 118612. [CrossRef] [PubMed]
6. Adonin, S.A.; Rakhmanova, M.E.; Samsonenko, D.G.; Sokolov, M.N.; Fedin, V.P. Bi (III) halide complexes containing 4,4′-vinylenedipyridinium cation: Synthesis, structure and luminescence in solid state. *Polyhedron* **2015**, *98*, 1–4. [CrossRef]
7. Lambarki, F.; Ouasri, A.; Zouihri, H.; Rhandour, A. Crystal structure, Hirshfeld and vibrational study at ambient temperature of propylammonium pentachlorobismuthate [n-C3H7NH3] 2BiCl5 (III). *J. Mol. Struct.* **2017**, *1142*, 275–284. [CrossRef]
8. Chański, M.; Białońska, A.; Jakubas, R.; Piecha-Bisiorek, A. Structural characterization and properties of bis (1, 4-H2-1, 2, 4-triazolium) pentachlorobismuthate (III) and cocrystal of ammonium chloride with tris (1, 4-H2-1, 2, 4-triazolium) hexachlorobismuthate (III). *Polyhedron* **2014**, *71*, 69–74. [CrossRef]
9. Ganguly, P.; Desiraju, G.R. Van der Waals and polar intermolecular contact distances: Quantifying supramolecular synthons. *Chem.–Asian J.* **2008**, *3*, 868–880. [CrossRef]

10. Ouerghi, Z.; Roisnel, T.; Fezai, R.; Kefi, R. Physico-chemical characterization, Hirshfeld surface analysis and opto-electric properties of a new hybrid material: Tris (2-amino-5-chloropyridinium) hexachlorobismuthate (III). *J. Mol. Struct.* **2018**, *1173*, 439–447. [CrossRef]

11. Zhu, S.; Jiang, M.; Ye, J.; Xie, H.; Qiu, Y. Optical properties of photovoltaic materials: Organic-inorganic mixed halide perovskites CH3NH3Pb (I1-yXy) 3 (X=Cl, Br). *Comput. Theor. Chem.* **2018**, *1144*, 1–8. [CrossRef]

12. Lyu, M.; Yun, J.-H.; Cai, M.; Jiao, Y.; Bernhardt, P.V.; Zhang, M.; Wang, Q.; Du, A.; Wang, H.; Liu, G. Organic–inorganic bismuth (III)-based material: A lead-free, air-stable and solution-processable light-absorber beyond organolead perovskites. *Nano Res.* **2016**, *9*, 692–702. [CrossRef]

13. Oswald, I.W.H.; Mozur, E.M.; Moseley, I.P.; Ahn, H.; Neilson, J.R. Hybrid Charge-Transfer Semiconductors: (C7H7)SbI4, (C7H7)BiI4, and Their Halide Congeners. *Inorg. Chem.* **2019**, *58*, 5818–5826. [CrossRef] [PubMed]

14. Qiu, Y.; Liu, W.; Chen, W.; Chen, W.; Zhou, G.; Hsu, P.-C.; Zhang, R.; Liang, Z.; Fan, S.; Zhang, Y. Efficient solar-driven water splitting by nanocone BiVO4-perovskite tandem cells. *Sci. Adv.* **2016**, *2*, e1501764. [CrossRef]

15. Ferjani, H. Structural, Hirshfeld surface analysis, morphological approach, and spectroscopic study of new hybrid iodobismuthate containing tetranuclear 0D cluster Bi4I16 4 (C6H9N2) 2 (H2O). *Crystals* **2020**, *10*, 397. [CrossRef]

16. Rhaiem, T.B.; Elleuch, S.; Boughzala, H.; Abid, Y. A new luminescent organic-inorganic hybrid material based on cadmium iodide. *Inorg. Chem. Commun.* **2019**, *109*, 107572. [CrossRef]

17. Ferjani, H.; Bechaieb, R.; Abd El-Fattah, W.; Fettouhi, M. Broad-band luminescence involving fluconazole antifungal drug in a lead-free bismuth iodide perovskite: Combined experimental and computational insights. *Spectrochim. Acta Part A Mol. Biomol. Spectrosc.* **2020**, *237*, 118354. [CrossRef]

18. Intissar, H.; Khan, Y.; Aouaini, F.; Seo, J.H.; Koo, H.-J.; Turnbull, M.M.; Walker, B.; Naïli, H. A Copper-Based 2D Hybrid Perovskite Solar Absorber as a Potential Eco-Friendly Alternative to Lead Halide Perovskites. *J. Mater. Chem. C* **2022**, *10*, 3738–3745.

19. Ferjani, H.; Boughzala, H. New Quasi-One-Dimensional Organic-Inorganic Hybrid Material: 1, 3-Bis (4-piperidinium) propane Pentachlorobismuthate (III) Synthesis, Crystal Structure, and Spectroscopic Studies. *J. Mater.* **2014**, *2014*, 253602. [CrossRef]

20. Ferjani, H.; Boughzala, H.; Driss, A. Poly [bis (1-carbamoylguanidinium)[tri-μ-chlorido-dichloridobismuthate (III)]]. *Acta Crystallogr. Sect. E Struct. Rep. Online* **2012**, *68*, m615. [CrossRef]

21. Bravais, A. *Etudes Cristallographiques*; Gauthier-Villars: France, Paris, 1866.

22. Donnay, J.; Harker, D. Springer Handbook of Crystal Growth. *Am. Mineral.* **1937**, *22*, 446–467.

23. Renjith, R.; Mary, Y.S.; Panicker, C.Y.; Varghese, H.T.; Pakosińska-Parys, M.; Van Alsenoy, C.; Manojkumar, T. Spectroscopic (FT-IR, FT-Raman), first order hyperpolarizability, NBO analysis, HOMO and LUMO analysis of 1,7,8,9-tetrachloro-10,10-dimethoxy-4-[3-(4-phenylpiperazin-1-yl)propyl]-4-azatricyclo[5.2.1.02,6]dec-8-ene-3,5-dione by density functional methods. *Spectrochim. Acta Part A Mol. Biomol. Spectrosc.* **2014**, *124*, 500–513. [CrossRef] [PubMed]

24. Jones, W.J. The infra-red spectrum and structure of guanidine. *Trans. Faraday Soc.* **1959**, *55*, 524–531. [CrossRef]

25. Jones, W.J.; Orville-Thomas, W. The infra-red spectrum and structure of dicyandiamide. *Trans. Faraday Soc.* **1959**, *55*, 193–202. [CrossRef]

26. Scoponi, M.; Polo, E.; Bertolasi, V.; Carassiti, V.; Bertelli, G. Crystal structure and spectroscopic analyses of guanylurea hydrochloride. Evidence of the influence of hydrogen bonding on the π-electron delocalization. *J. Chem. Soc. Perkin Trans.* **1991**, *2*, 1619–1624. [CrossRef]

27. Matulková, I.; Fridrichová, M.; Císařová, I.; Vaněk, P.; Uhlík, F.; Němec, I. Vibrational spectroscopic and crystallographic study of the novel guanylurea salts with sulphuric and selenic acids. *J. Mol. Struct.* **2017**, *1131*, 294–305. [CrossRef]

28. Rao, A.S.; Baruah, U.; Das, S.K. Stabilization of [BiCl6] 3− and [Bi2Cl10] 4− with various organic precursors as cations leading to inorganic–organic supramolecular adducts: Syntheses, crystal structures and properties of [C5H7N2] 3 [BiCl6],[C5H7N2][C5H8N2][BiCl6] and [C10H10N2] 2 [Bi2Cl10]. *Inorg. Chim. Acta* **2011**, *372*, 206–212.

29. Oldenburg, K.; Vogler, A.; Mikó, I.; Horváth, O. Photoredox decomposition of tin (II), lead (II), antimony (III) and bismuth (III) iodide complexes in solution. *Inorg. Chim. Acta* **1996**, *248*, 107–110. [CrossRef]

30. Clark, S.J.; Segall, M.D.; Pickard, C.J.; Hasnip, P.J.; Probert, M.I.; Refson, K.; Payne, M.C. First principles methods using CASTEP. *Z. Für Krist.-Cryst. Mater.* **2005**, *220*, 567–570. [CrossRef]

31. Vogler, A.; Nikol, H. Photochemistry and photophysics of coordination compounds of the main group metals. *Pure Appl. Chem.* **1992**, *64*, 1311–1317. [CrossRef]

32. Moore, C.H. *Coordination Chemistry of Guanidine Derivatives*; University of Nottingham: Nottingham, UK, 1989.

33. Badgujar, D.M.; Wagh, R.M.; Pawar, S.J.; Sikder, A.K. Process optimization for synthesis of guanylurea dinitramide (GUDN). *Propellants Explos. Pyrotech.* **2014**, *39*, 658–661. [CrossRef]

34. Wu, L.-M.; Wu, X.-T.; Chen, L. Structural overview and structure–property relationships of iodoplumbate and iodobismuthate. *Coord. Chem. Rev.* **2009**, *253*, 2787–2804. [CrossRef]

35. Adonin, S.A.; Sokolov, M.N.; Fedin, V.P. Polynuclear halide complexes of Bi (III): From structural diversity to the new properties. *Coord. Chem. Rev.* **2016**, *312*, 1–21. [CrossRef]

36. Ferjani, H.; Boughzala, H.; Driss, A. Synthesis, Crystal Structure, and Characterization of a New Organic-Inorganic Hybrid Material. *J. Crystallogr.* **2013**, *2013*, 658939. [CrossRef]

37. Pelle, F.; Jacquier, B.; Denis, J.; Blanzat, B. Optical properties of Cs2NaBiCl6. *J. Lumin.* **1978**, *17*, 61–72. [CrossRef]

38. Chang, L.; Besteiro, L.V.; Sun, J.; Santiago, E.Y.; Gray, S.K.; Wang, Z.; Govorov, A.O. Electronic structure of the plasmons in metal nanocrystals: Fundamental limitations for the energy efficiency of hot electron generation. *ACS Energy Lett.* **2019**, *4*, 2552–2568. [CrossRef]

39. Toll, J.S. Causality and the dispersion relation: Logical foundations. *Phys. Rev.* **1956**, *104*, 1760. [CrossRef]

40. Gajdoš, M.; Hummer, K.; Kresse, G.; Furthmüller, J.; Bechstedt, F. Linear optical properties in the projector-augmented wave methodology. *Phys. Rev. B* **2006**, *73*, 045112. [CrossRef]

41. Yu, P.Y.; Cardona, M. Electronic band structures. In *Fundamentals of Semiconductors*; Springer: Berlin/Heidelberg, Germany, 2010; pp. 17–106.

42. Cardona, M.; Peter, Y.Y. *Fundamentals of Semiconductors*; Springer: Berlin/Heidelberg, Germany, 2005; Volume 619.

43. Crespo, C.T. The effect of the halide anion on the optical properties of lead halide perovskites. *Sol. Energy Mater. Sol. Cells* **2019**, *195*, 269–273. [CrossRef]

44. Liu, S.; Wang, J.; Hu, Z.; Duan, Z.; Zhang, H.; Zhang, W.; Guo, R.; Xie, F. Role of organic cation orientation in formamidine based perovskite materials. *Sci. Rep.* **2021**, *11*, 20433. [CrossRef]

45. Pazoki, M.; Johansson, M.B.; Zhu, H.; Broqvist, P.; Edvinsson, T.; Boschloo, G.; Johansson, E.M. Bismuth iodide perovskite materials for solar cell applications: Electronic structure, optical transitions, and directional charge transport. *J. Phys. Chem. C* **2016**, *120*, 29039–29046. [CrossRef]

46. Alnujaim, S.; Bouhemadou, A.; Bedjaoui, A.; Bin-Omran, S.; Al-Douri, Y.; Khenata, R.; Maabed, S. Ab initio prediction of the elastic, electronic and optical properties of a new family of diamond-like semiconductors, Li2HgMS4 (M=Si, Ge and Sn). *J. Alloys Compd.* **2020**, *843*, 155991. [CrossRef]

47. Perdew, J.P.; Ruzsinszky, A.; Csonka, G.I.; Vydrov, O.A.; Scuseria, G.E.; Constantin, L.A.; Zhou, X.; Burke, K. Restoring the density-gradient expansion for exchange in solids and surfaces. *Phys. Rev. Lett.* **2008**, *100*, 136406. [CrossRef] [PubMed]

48. Vanderbilt, D. Soft self-consistent pseudopotentials in a generalized eigenvalue formalism. *Phys. Rev. B* **1990**, *41*, 7892. [CrossRef]

49. Monkhorst, H.J.; Pack, J.D. Special points for Brillouin-zone integrations. *Phys. Rev. B* **1976**, *13*, 5188. [CrossRef]

50. Spackman, M.; Jayatilaka, D. Hirshfeld Surface Analysis. *CrystEngComm* **2009**, *11*, 19–32. [CrossRef]

51. Spackman, M.A.; Spackman, P.R.; Thomas, S.P. Beyond Hirshfeld Surface Analysis: Interaction Energies, Energy Frameworks and Lattice Energies with CrystalExplorer. *Complementary Bond. Anal. Gruyter* **2021**, 329–352. [CrossRef]

52. Jelsch, C.; Ejsmont, K.; Huder, L. The enrichment ratio of atomic contacts in crystals, an indicator derived from the Hirshfeld surface analysis. *IUCrJ* **2014**, *1*, 119–128. [CrossRef]

53. *Materials Studio, Version 7.0*; Accelrys Software Inc.: San Diego, CA, USA, 2013.